First-in-class humanized FSH blocking antibody targets bone and fat

Sakshi Gera[a], Damini Sant[a], Shozeb Haider[b], Funda Korkmaz[a], Tan-Chun Kuo[a], Mehr Mathew[a], Helena Perez-Pena[b], Honglin Xie[c], Hao Chen[d], Rogerio Batista[a], Kejun Ma[a,e], Zhen Cheng[d], Elina Hadelia[a], Cemre Robinson[a], Anne Macdonald[a], Sari Miyashita[a], Anthony Williams[a], Gregory Jebian[a], Hirotaka Miyashita[a], Anisa Gumerova[a], Kseniia Ievleva[a], Pinar Smith[a], Jiahuan He[f], Vitaly Ryu[a], Victoria DeMambro[g], Matthew A. Quinn[h], Marcia Meseck[i], Se-Min Kim[a], T. Rajendra Kumar[j], Jameel Iqbal[a], Maria I. New[k,1], Daria Lizneva[a], Clifford J. Rosen[g], Aaron J. Hsueh[f], Tony Yuen[a], and Mone Zaidi[a,1]

[a]The Mount Sinai Bone Program, Department of Medicine, Icahn School of Medicine at Mount Sinai, New York, NY 10029; [b]Department of Pharmaceutical and Biological Chemistry, University College London School of Pharmacy, WC1N 1AX London, United Kingdom; [c]GenScript Biotech Corporation, Piscataway, NJ 08854; [d]Molecular Imaging Program at Stanford, Bio-X Program, Department of Radiology, Stanford University, Stanford, CA 94305; [e]Cuiying Biomedical Research Center, Lanzhou University Second Hospital, Lanzhou, Gansu 730030, China; [f]Department of Obstetrics and Gynecology, Stanford University School of Medicine, Stanford, CA 94305; [g]Center for Clinical and Translational Research, Maine Medical Center Research Institute, Scarborough, ME 04074; [h]Department of Pathology, Wake Forest School of Medicine, Winston-Salem, NC 27157; [i]Tisch Cancer Institute, Icahn School of Medicine at Mount Sinai, New York, NY 10029; [j]Department of Obstetrics and Gynecology, University of Colorado School of Medicine, Aurora, CO 80045; and [k]Department of Pediatrics, Icahn School of Medicine at Mount Sinai, New York, NY 10029

Contributed by Maria I. New, September 2, 2020 (sent for review July 13, 2020; reviewed by Xu Cao, Christopher Huang, and Carlos Isales)

Blocking the action of FSH genetically or pharmacologically in mice reduces body fat, lowers serum cholesterol, and increases bone mass, making an anti-FSH agent a potential therapeutic for three global epidemics: obesity, osteoporosis, and hypercholesterolemia. Here, we report the generation, structure, and function of a first-in-class, fully humanized, epitope-specific FSH blocking antibody with a K_D of 7 nM. Protein thermal shift, molecular dynamics, and fine mapping of the FSH–FSH receptor interface confirm stable binding of the Fab domain to two of five receptor-interacting residues of the FSHβ subunit, which is sufficient to block its interaction with the FSH receptor. In doing so, the humanized antibody profoundly inhibited FSH action in cell-based assays, a prelude to further preclinical and clinical testing.

monoclonal antibody | humanization | follicle-stimulating hormone | adipose

Obesity and osteoporosis affect nearly 650 million and 200 million people worldwide, respectively (1, 2). Yet the armamentarium for preventing and treating these disorders remains limited, particularly when compared with public health epidemics of a similar magnitude. It has also become increasingly clear that obesity and osteoporosis track together clinically. First, body mass does not protect against bone loss; instead, obesity can be permissive to osteoporosis and a high fracture risk (3, 4). Furthermore, the menopausal transition marks the onset not only of rapid bone loss, but also of visceral obesity and dysregulated energy balance (5–9). These physiologic aberrations have been attributed traditionally to a decline in serum estrogen, although, during the perimenopause—2 to 3 y prior to the last menstrual period—serum estrogen is within the normal range, while FSH levels rise to compensate for reduced ovarian reserve (10–12). In our view, therefore, the early skeletal and metabolic derangements cannot conceivably be explained solely by declining estrogen (13, 14).

The past decade has shown that pituitary hormones can act directly on the skeleton and other tissues, a paradigm shift that is in stark contrast to previously held views on their sole regulation of endocrine targets (15–25). We and others have shown that FSH can bypass the ovary to act on G_i-coupled FSH receptors (FSHRs) on osteoclasts to stimulate bone resorption and inhibit bone formation (26, 27). This mechanism, which could underscore the bone loss during early menopause, is testified by the strong correlations between serum FSH, bone turnover, and bone mineral density (7–9, 14, 16, 26). Likewise, activating polymorphisms in the *FSHR* in postmenopausal women are linked to a high bone turnover and reduced bone mass (27). It therefore made biological and clinical sense to inhibit FSH action during this period to prevent bone loss.

Toward this goal, we generated murine polyclonal and monoclonal antibodies to a 13-amino-acid–long binding epitope of FSHβ (28–31). The mouse and human FSHβ epitopes differ by just two amino acids; hence, blocking antibodies to the human epitope showed efficacy in mice (28). The antibodies displayed two sets of actions: they attenuated the loss of bone after ovariectomy by inhibiting bone resorption and stimulating bone formation and displayed profound effects on body composition and energy metabolism (28, 29, 31). Most notably, in a series of contemporaneously reproduced experiments, we (M.Z. and C.J.R.) found that FSH blockade reduced body fat, triggered adipocyte beiging, and increased thermogenesis in models of obesity, notably post ovariectomy and after high-fat diet (29). Our findings have been further confirmed independently by two groups who used a FSHβ–GST fusion protein or tandem repeats

Significance

We report the development and characterization of a first-in-class humanized antibody to follicle-stimulating hormone (FSH). We have shown previously that blocking FSH action on its receptor increases bone mass, reduces body fat, and enhances energy expenditure. Furthermore, FSH has been reported to increase serum cholesterol. Therefore, an anti-FSH agent has the potential of preventing and treating obesity, osteoporosis, and hypercholesterolemia, diseases that affect millions of women and men worldwide. Our study provides the framework for further preclinical and subsequent clinical testing of our humanized antibody to FSH.

Author contributions: S.H., H.X., M.I.N., C.J.R., A.J.H., T.Y., and M.Z. designed research; S.G., D.S., S.H., F.K., T.-C.K., M. Mathew, H.P.-P., H.X., H.C., K.M., Z.C., E.H., A.W., G.J., A.G., K.I., J.H., V.D., and D.L. performed research; S.G., D.S., S.H., T.-C.K., H.X., H.C., R.B., Z.C., E.H., C.R., A.M., S.M., H.M., P.S., V.R., V.D., M.A.Q., M. Meseck, S.-M.K., T.R.K., J.I., D.L., T.Y., and M.Z. analyzed data; and M.I.N., T.Y., and M.Z. wrote the paper.

Reviewers: X.C., Johns Hopkins School of Medicine; C.H., University of Cambridge; and C.I., Augusta University.

The authors declare no competing interest.

[1]To whom correspondence may be addressed. Email: maria.new@mssm.edu or mone.zaidi@mssm.edu.

This article contains supporting information online at https://www.pnas.org/lookup/suppl/doi:10.1073/pnas.2014588117/-/DCSupplemental.

First published October 30, 2020.

of the 13-amino-acid–long FSHβ epitope for studies on bone and fat, respectively (32, 33). Consistent with the mouse data, inhibiting FSH secretion using a GnRH agonist in prostate cancer patients resulted in low body fat compared with orchiectomy, wherein FSH levels are high (34). This interventional clinical trial provides evidence for a therapeutic benefit of reducing FSH levels on body fat in people. There is also new evidence that FSH blockade lowers serum cholesterol (35, 36).

Thus, both emerging and validated datasets on the antiobesity, osteoprotective, and lipid-lowering actions of FSH blockade in mice and in humans prompted our current attempt to develop and characterize an array of fully humanized FSH-blocking antibodies for future testing in people. Here, we report that our lead first-in-class humanized antibody, Hu6, and two related molecules, Hu26 and Hu28, bind human FSH with a high affinity (K_Ds <10 nM), block the binding of FSH on the human FSHR, and inhibit FSH action in functional cell-based assays.

Results

First-in-Class Humanized Anti-FSHβ Antibodies. Two murine monoclonal anti-FSHβ antibodies, Mf4 and Hf2, developed by us against corresponding mouse and human receptor-binding epitopes of the ligand FSHβ, namely LVYKDPARPNTQK and LVYKDPARPKIQK, were validated for biological efficacy in enhancing bone mass in ovariectomized mice (28), and, in the case of Hf2, in reducing body fat and inducing adipocyte beiging (29). When tested for their ability to inhibit osteoclast formation in a cell-based assay, the antibodies displayed IC_{50}s of 5.4 and 6.1 nM, respectively (28). Hf2 was selected for humanization and further testing.

The variable domains of the heavy and light IgG chains, V_H and V_L, were amplified from Hf2 hybridomas. A mouse–human chimeric antibody (CH1) was first constructed by cloning the corresponding V_H and V_L together with human IgG_1-C_H and IgK-C_L fragments, respectively, into pTT5 vector. To generate fully humanized antibodies, a bacterial expression library consisting of the antigen-binding fragments (Fab) was produced with single site mutations introduced in the human framework flanking the complementarity-determining region (CDR) while keeping the CDR itself unaltered. This yielded 30 humanized Fab clones (1-30), which were expressed in *Escherichia coli*. Crude supernatant extracts were initially tested for binding to both mouse and human FSHβ in an ELISA (*SI Appendix*, Fig. S1), followed by further confirmation of FSH binding by surface plasma resonance (SPR; Biacore) and rank-ordering by dissociation constants (K_ds; *SI Appendix*, Table S1). Three full-length high-affinity humanized IgGs with the lowest K_ds were purified (*SI Appendix*, Fig. S2*A*); these are henceforth referred to as Hu6, Hu26, and Hu28. For Hu6, we also digested with papain to produce the Fab and Fc fragments (*SI Appendix*, Fig. S2*B*)

Highly Specific Binding of Hu6, Hu26, and Hu28 to Human FSH. We utilized three complementary approaches to establish the binding of Hu6, Hu26, and Hu28, as well as CH1 to recombinant mouse and human FSH. SPR yielded binding affinities (K_Ds) of 7.52, 10.5, and 12.8 nM to human FSH for Hu6, Hu26, and Hu28, respectively (Fig. 1 *A* and *B*). The respective antibodies also bound mouse FSHβ with somewhat higher affinities (Fig. 1*B* and *SI Appendix*, Fig. S3). Such cross-reactivity was expected, as the human epitope to which the antibodies were raised was different by just two amino acids from the mouse sequence (NT→KI) (28), thus allowing us to use murine cell-based models for efficacy testing of the humanized molecule.

We further tested the specificity of binding of the full-length antibody and/or its Fab and Fc fragments to pituitary-derived human FSH and its recombinant glycoforms by ELISA. $FSH^{21/18}$ is a combination of glycoforms that are N-glycosylated at Asn^7 or Asn^{24} of FSHβ, respectively, whereas fully glycosylated FSH^{24} contains an N-glycan at both residues. Plates were coated with equal concentrations of human FSH, $FSH^{21/18}$, FSH^{24}, LH, or TSH (50 ng each). Binding was assessed using an HRP-conjugated antibody to human IgG following overnight incubation with increasing concentrations of Hu6, Hu6-Fab, Hu6-Fc, Hu26, Hu28, or CH1. Fig. 1*C* shows concentration-dependent binding of our humanized antibodies to FSH, whereas no binding was detected with LH or TSH or when control human IgG was used. However, Hu26 and Hu28 bound more avidly to $FSH^{21/18}$ compared with FSH^{24}; the concentration–response curves of Hu6 with FSH glycoforms were almost overlapping. Of note is that serum FSH^{24} levels are known to rise with biological aging (37), suggesting that fully glycosylated FSH^{24} may be the major regulator of extragonadal actions of FSH on bone and fat. Indeed, in differentiating 3T3.L1 adipocytes, we have found repeatedly that FSH^{24}, but not $FSH^{21/18}$, inhibits the cAMP response to the β_3 adrenergic agonist CL316,243 (Fig. 1*D*) (29). Finally, we found expectedly that the Fab, but not the Fc, fragment of Hu6 (purity shown in *SI Appendix*, Fig. S2*B*) displayed FSH binding (Fig. 1*C*).

We finally confirmed binding of our lead molecule, Hu6, as well as its Fab fragment, with a protein thermal-shift assay that utilizes a fluorescent reporter to detect hydrophobic domains that are exposed following the unfolding of globular proteins with increasing temperature. In the presence of ligand, protein structure is stabilized, requiring a higher temperature for it to unfold. Hu6, Hu6-Fab, or Hu6-Fc were incubated with or without human FSH in the presence of Sypro-Orange (Applied Biosystems) at room temperature for 30 min. Fluorescence was captured sequentially at 0.3 °C increments using a StepOne Plus Thermocycler (Applied Biosystems). FSH, a protein composed mainly of β-sheets, expectedly showed no increase in fluorescence upon heating. In contrast, Hu6 showed two peaks: one at ∼69 °C representing unfolding of the Fc domain and another at 77 °C resulting from unfolding of the Fab region (Fig. 1*E*). Incubation of Hu6 with human FSH produced a dramatic, ∼6 °C, right shift of the Fab peak, but not the Fc peak. The persistence of the right shift at 83 °C was consistent with a stable high-affinity binding of FSH to the Fab domain (Fig. 1*E*). This was confirmed by assaying the Fab and Fc fragments separately. Whereas Hu6-Fab showed a right shift (3 °C) when incubated with FSH, no such thermal shift was observed with Hu6-Fc (Fig. 1*E*); this confirmed our ELISA results (above; Fig. 1*C*). Of note, and consistent with ELISA (Fig. 1*C*), human LH failed to produce a thermal shift (Fig. 1*E*).

Atom-Level Fine Mapping of Antibody–FSH Interactions. To study the interaction of Hu6, Hu23, Hu26, Hu28, and CH1 clones with human and mouse FSHβ in atomistic detail, we modeled the respective variable regions of each antibody clone using Modeler 9.1 (38). The antibody–FSHβ interacting interface was then studied by HADDOCK (39, 40). To identify interactions that stabilized docked antibody–FSHβ complexes, each complex was subjected to molecular dynamics simulations. rmsd-based clustering identified three clusters, from which the medoid was selected to calculate electrostatic energy (using APBS). Of note is that, while the CDR regions of Hu6, Hu23, Hu26, and Hu28 are identical, mutations in the flanking region of the CDRs created during humanization caused subtle differences in the FSHβ residues that were recognized by the antibodies (below).

Both V_H and V_L regions of the antibody clones interacted with the targeted epitope residues of human and mouse FSHβ, with predicted electrostatic energies (ΔΔGs) consistent with K_Ds calculated from the SPR dataset (Fig. 2 *A* and *B*). Both human and mouse FSHβ epitopes and V_L region of CH1 displayed the most electrostatic interactions (Fig. 2 *A* and *B* and *SI Appendix*, Fig. S4). However, whereas there were no direct interactions between K46 of human FSHβ and CH1, with mouse FSHβ, residue N46 interacted with R44 that then interacted with D104

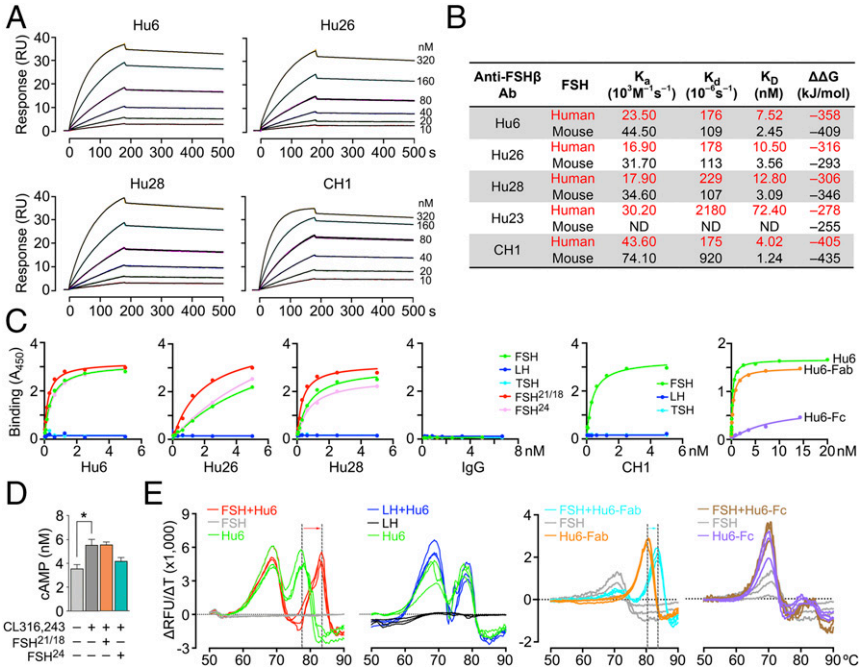

Anti-FSHβ Ab	FSH	K_a ($10^3 M^{-1}s^{-1}$)	K_d ($10^{-6}s^{-1}$)	K_D (nM)	ΔΔG (kJ/mol)
Hu6	Human	23.50	176	7.52	−358
	Mouse	44.50	109	2.45	−409
Hu26	Human	16.90	178	10.50	−316
	Mouse	31.70	113	3.56	−293
Hu28	Human	17.90	229	12.80	−306
	Mouse	34.60	107	3.09	−346
Hu23	Human	30.20	2180	72.40	−278
	Mouse	ND	ND	ND	−255
CH1	Human	43.60	175	4.02	−405
	Mouse	74.10	920	1.24	−435

Fig. 1. Humanized anti-FSHβ antibodies specifically bind human FSH. Surface plasmon resonance (SPR, Biacore 8K/T200) was utilized to study the binding properties of human and mouse FSH with the purified humanized antibodies Hu6, Hu26, Hu28, and Hu23, as well as human–mouse chimeric molecule CH1. (*A*) Sensograms showing the concentration-dependent binding of humanized antibodies Hu6, Hu26, and Hu28 (10 to 320 nM) to human FSH. (*B*) SPR yielded measures of association constant (K_a), dissociation constant (K_d) and affinity (K_D). The K_D values were consistent with in silico global net electrostatic binding energies (DDG) calculated from molecular dynamics using APBS. Hu6 displayed the highest K_D and lowest K_d and was thus chosen as the lead molecule for development. ND – not determined. Please also refer to *SI Appendix*, Fig. S3. (*C*) ELISA showing binding of Hu6, Hu6-Fab, Hu26, Hu28, or CH1 to pituitary-derived human FSH and its recombinant glycoforms, $FSH^{21/18}$ and FSH^{24}, but not to human LH, human TSH (coating at 50 ng), or Hu6-Fc detected with HRP-conjugated antibody to human IgG. There is no binding with human IgG. Data are a mean of duplicate wells. (*D*) cAMP production in differentiated 3T3.L1 cells incubated with $FSH^{21/18}$ or FSH^{24} in the presence of the β_3 agonist CL316,243 ($n = 3$ biological replicates). (*E*) Protein thermal shift assay utilizes Sypro-Orange to capture hydrophobic domains during heat-induced protein unfolding to yield a melting temperature (Tm). Change in fluorescence is shown as relative fluorescence units (ΔRFU) per unit change in temperature (ΔT). Hu6 showed two peaks: one at ~69 °C, predicted to be caused by unfolding of the Fc domain, and the other at 77 °C, likely due to unfolding of Fab region. The addition of human FSH, but not human LH, produced a thermal shift solely in the putative Fab peak. Binding of FSH to the Fab domain was confirmed by a comparable thermal shift in Hu6-Fab, but not Hu6-Fc, in the presence of FSH.

and Y105 of the V_H region. This latter pattern of atomistic interactions between antibody and residue K/N46 broadly resembled that of Hu6 (Fig. 2 *A* and *B* and *SI Appendix*, Fig. S4). With clone Hu26, in the human complex, K46 made direct hydrogen bonds with D28, S30, and H92 of the V_L region (Fig. 2 *A* and *B*). In the mouse complex, whereas residue N46 did not directly interact with V_L, it interacted with the guanidinium side chain of R44, which, in turn, interacted with S30, Y32, and H92 (Fig. 2*A* and *SI Appendix*, Fig. S4). Clone Hu28 displayed lesser affinity and reduced interactions with both human and mouse FSHβ (Fig. 1*B*, Fig. 2*A*, Fig. 2*B*, and *SI Appendix*, Fig. S4). The side chain of residue N46 of mouse FSHβ (and not K46 of human FSHβ) interacted directly with residue Y32 of the V_L region. Displaying the least ΔΔG (Fig. 1*B*), Hu23 interacted minimally with mouse and human FSHβ (Fig. 2*A*, Fig. 2*B*, and *SI Appendix*, Fig. S4). Specifically, residue K/N46 did not interact with the V_L region of Hu23. However, the R44 side chain of the mouse complex formed a hydrogen bond with Y32, and the carbonyl oxygen of the backbone of P42 interacted with R53 of V_L.

It is interesting that, while the humanized molecules were developed using the parent antibody, Hf2, designed against the human FSHβ epitope (28), all clones showed favorable affinities toward mouse FSHβ, which was different in just two amino acids (NT→KI; Fig. 1*B*). One explanation is that, with mouse FSHβ, the smaller size of N46 permits direct interactions with the V_L chain of the antibodies; if not, it forms hydrogen bonds with the guanidinium side chain of R44. This internal electrostatic interaction within mouse FSHβ stabilizes the loop structure of its epitope, thus allowing more favorable interactions. In contrast, in the case of human FSHβ, the relatively longer K46 side chain is unable to make internal interactions, resulting in charge repulsion with R44. This leads to destabilization of the loop structure, causing fewer interactions between the human FSHβ chain and the respective antibodies. Thus, the structure adopted by the epitope sequence and its side chain determines the ability to make inter- and intra-electrostatic interactions.

We independently explored the validity of in silico interactions between amino acid residues of FSH and antibody by determining whether or not the interacting Fab residues were solvent-exposed. If these were found to be buried within the structure, the interaction would be invalidated. The modeled structures of the Fab domain of Hu6, Hu23, Hu26, Hu28, and CH1 were thus inputted into GETAREA to derive estimates of solvent-accessible surface area (SASA; Fig. 2*C*). SASA estimates of <20 indicate a buried amino acid residue. For the three CDR regions (shown in red in Fig. 2*C*), all interacting amino acids displayed SASA values of ≥20 (range, 20 to 95). For example, FSH residue K46 bonded with D28, S30, and H92 residues of Hu26, all of which were solvent-accessible with SASAs of 83, 84, and 48.

Hu6, H26, and Hu28 Block FSH–FSHR Interactions. Having fine-mapped the binding interface of the humanized antibodies to FSH, we tested experimentally whether the antibodies blocked the interaction of FSH with its receptor. For this, we created a stable FSHR-overexpressing HEK293 cell line, wherein FSHR was detected by flow cytometry using Alexa 647-labeled human FSH

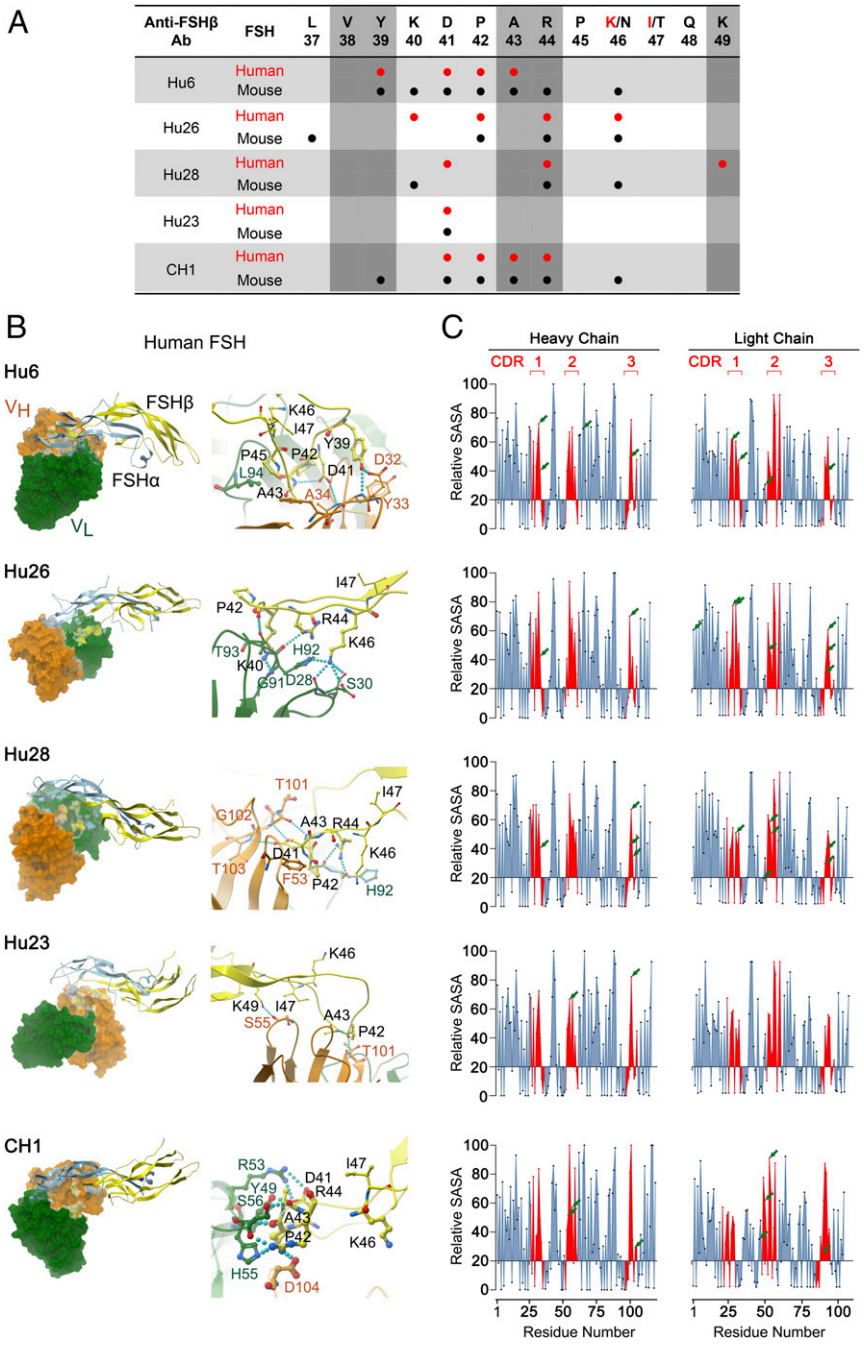

Fig. 2. Atom-level fine mapping of antibody–FSH interfaces and solvent accessibility of Interacting residues. (*A*) In silico fine mapping of residues of the targeted 13-amino-acid–long human or mouse FSHβ epitope that interact with specific residues of the variable chain of the antibodies Hu6, Hu26, Hu28, and Hu23, as well as the mouse–human chimera (CH1). The five residues that are known to interact with the FSHR (28) have been identified by vertical shades. (*B*) Shown are computational models and fine maps of complexes between the α (blue) and β (yellow) subunits of human FSH and the variable regions, V_L (green) and V_H (orange), of the antibodies. Interactions between specific amino acids are shown (*SI Appendix*, Fig. S4). (*C*) Calculated relative SASA values [derived from GETAREA (57, 58); *Methods*] of individual amino acids within V_H and V_L regions, with CDRs shown in red. Values below 20 represent an "in" configuration on GETAREA, which reflects solvent-inaccessible (buried) residues. Residues that interact with human FSH are shown by arrows, with ~70% having SASAs ≥50, indicating good solvent accessibility.

(*FSH) or an anti-FSHR antibody (1 in 1,000; Invitrogen, PA-50963; Fig. 3). Hu6, Hu26, and Hu28 and the chimera CH1 all prevented *FSH binding to FSHR-overexpressing HEK293 cells in three separate experiments (Fig. 3). Namely, there was a right shift in fluorescence intensity with *FSH, and this shift was reversed with all FSH-blocking antibodies, including our polyclonal antibody (positive control), but not with human IgG (Fig. 3). Of note is that the relatively high concentration (100 nM) of *FSH required for eliciting a fluorescence signal might result from a reduced affinity arising from the labeling of Lys residues (K40, K46, and K49) within the binding site. The data establish that our antibodies effectively block FSH action on the FSHR.

Plasma Half-Life and Cellular Actions of Hu6. Given our interest in utilizing our lead humanized anti-FSH antibody Hu6 for the treatment of osteoporosis and obesity, we measured its plasma

half-life ($t_{1/2}$) and used two cell-based assays to study its FSH blocking action. A single dose of Hu6 (100 μg) injected intraperitoneally into C57BL/6J mice ($n = 6$) was followed by blood draws at 2 h post-injection and thereafter at 24-h intervals. Serum Hu6 levels were measured by an in-house ELISA, in which plates were coated with goat anti-human IgG Fab (200 μg per well; Invitrogen, no. 31122) followed by capture by a different goat anti-human HRP-conjugated IgG (H + L; Invitrogen, A18805). A C_{max} value of 20.5 μg/mL was achieved at 2 h, yielding a $t_{1/2}$ of 34.3 h (Fig. 4*A*). This is consistent with previous estimates for our polyclonal anti-FSH antibody raised in goat (29). Noting the long $t_{1/2}$ of Hu6 in the mouse, it was imperative that we determine whether FSH inhibition evoked a rise in serum LH. In a separate experiment, blood was drawn at day 0, following which groups of mice ($n = 5$ mice per group) received either one injection or two injections 48 h apart of Hu6 or human IgG (100 μg per mouse). There were no significant differences in serum FSH, LH, activin A, or total inhibin levels (Fig. 4*B*), suggesting that Hu6 is unlikely to cause hyperandrogenemia due to elevated LH production, akin to *Fshb* haploinsufficiency from birth to maturity (41). It is equally important to stress that GnRH agonists used in clinical studies (13, 42, 43) reduce LH levels with downstream effects on other reproductive hormones, making any negative outcome fraught with multiple confounding variables, and therefore, at best, uninterpretable.

We next examined whether our panel of humanized antibodies inhibited FSH-induced osteoclast formation. Bone marrow hematopoietic cells were incubated with RANKL (100 ng/mL) and MCSF (20 ng/mL) for 5 d with or without FSH (50 ng/mL) and increasing antibody concentrations. As FBS-containing medium was used, we expected that each antibody, by blocking the action of endogenous FSH [up to 78 ng/mL (44)], would reduce osteoclast numbers, quantitated as ACP5-positive cells, in the absence of added FSH, and this was indeed the case (Fig. 4 *C* and *D*). The IC_{50}s of the three antibodies were in the subnanomolar range (Fig. 4*C*).

To establish FSH specificity, we first spiked the medium with 50 ng/mL FSH and found that the stimulation by FSH of osteoclastogenesis was attenuated with increasing antibody concentrations (Fig. 4 *C* and *D*). Second, we utilized bone marrow cell cultures from $Fshr^{-/-}$ mice, which displayed a reduced propensity to form osteoclasts; the latter finding confirmed an inhibitory effect of FSHR deletion per se on osteoclastogenesis (Fig. 4*E*). More importantly, however, while all three antibodies suppressed osteoclast formation in wild type cultures compared with IgG, they failed to further suppress osteoclastogenesis in $Fshr^{-/-}$ cultures (Fig. 4*E*). Together, the findings prove that Hu6, Hu26, and Hu28 inhibit osteoclast formation by blocking FSH signaling, a prelude for their testing for osteoprotection in people.

In a second assay, we explored the effects of Hu6 on expression of adipocyte beiging genes in 3T3.L1 cells. Cells were differentiated in the presence of FBS (10%, vol/vol), rosiglitazone (0.5 μM), dexamethasone (0.25 μM), IBMX (0.125 mM), and insulin (2.5 μg/mL). FSH caused a significant reduction in the expression of *Cox8b*, *Ucp1*, and *Prdm16*, but not *Cebpa* (Fig. 4*F*). Importantly, whereas Hu6 (6.6 nM) itself had no significant effect on gene expression, it reversed the inhibition noted at both FSH concentrations (10 and 30 ng/mL; Fig. 4*F*). This effect, consistent with our proof-of-concept polyclonal antibody data (29), provides the framework for studying the pro-beiging and thermogenic efficacy of Hu6 in in vivo models.

Indeed, we have shown previously, using real-time PCR and/or Sanger sequencing, that *Fshr*s are expressed in 3T3.L1 cells, primary adipocytes, and mouse adipose tissue (29). For direct confirmation that FSH binds these receptors, we (A.J.H.) utilized FSH-CH, a synthetic conjugate of human FSH and CH1055; the latter is a near-infrared II (NIR-II) fluorophore. Incubation of 3T3-L1 cells with FSH-CH resulted in a concentration-dependent increase in the NIR-II signal, which was attenuated strongly upon addition of a 100-fold molar access, i.e., 42 μg/mL, of nonconjugated FSH (K_D, 3.7 nM; Fig. 4*G*). We further confirmed binding to fat tissue in BALB/c mice injected with FSH-CH with or without 30× unconjugated FSH. NIR-II signals were detected in the ovaries, skeleton, liver, and white and brown adipose tissue; these signals were attenuated in the presence of excess unconjugated FSH, confirming specificity (*SI Appendix*, Fig. S5).

Discussion

Here we report the development of, and a full compendium of structural and functional studies on, a first-in-class humanized FSH-blocking antibody targeted to a 13-amino-acid–long receptor-binding epitope of the FSHβ subunit. We have shown previously that targeting this sequence blocks the binding of FSHβ to the FSHR, and, in doing so, inhibits bone resorption, promotes bone formation, increases bone mass, reduces body fat, and enhances thermogenesis in mice (29–31). Recent contemporaneous studies using a GST–FSHβ fusion protein or tandem repeats of the epitope provide confirmatory evidence for osteoprotection and weight loss (32, 33). Given the mounting evidence across species for direct actions of FSH on bone (19, 28, 29, 31, 33), adipose tissue (29, 32, 45, 46), and liver (35, 36), we sought to create a single FSH-blocking agent to treat three global epidemics that affect millions of women and men, namely obesity, osteoporosis, and hyperlipidemia. We therefore humanized our murine monoclonal antibody, Hf2, which was raised against a corresponding human FSHβ sequence (28). This generated 30 clones, from which we selected our lead molecule, Hu6, with the highest affinity and lowest dissociation constant.

We chose not to target full-length FSHβ; instead, we fine-mapped the receptor binding sequence from the available human cocrystal (PDB ID code 4AY9) and our computational model of the mouse complex (28, 30, 31). With largely similar binding modes, we mapped V38, Y39, A43, R44, and K49 as the only receptor-interacting residues in the human FSHβ sequence, with an additional interaction of residue D41 in the mouse (28). Here, we find that Hu6 binds two of these interacting residues, Y39 and A43, whereas Hu28 binds R44 and K49. In contrast, Hu26 and Hu23 bind only a single interacting residue. Thus, by purposefully creating atom-level maps between FSH and FSHR (28) and between FSH and the antibodies, we were able to confirm Hu6, which bound two centrally positioned residues, as our lead molecule. Its affinity of ∼7 nM is close to that of the HER2 blocker trastuzumab (K_D ∼5 nM) (47). A higher affinity might not be required, as *Fshr* haploinsufficiency phenocopies the effect of blocking FSH with our antibodies (29).

We further utilized complementary methods, namely ELISA, SPR, and, importantly, the protein thermal shift assay, to document unequivocally the binding of the Fab domain of Hu6 (and other humanized versions) to human FSH. Likewise, we show that Hu6 blocks FSH from binding to the FSHR, and, in doing so, inhibits FSH action in functional cell-based assays for osteoclast formation and beiging gene expression. We propose now to take Hu6 as a lead molecule into in vivo efficacy and safety testing and clinical development, with the ultimate goal of cotreating osteoporosis, obesity, and hyperlipidemia with a single agent.

Correlations between the onset of bone loss and visceral obesity during the menopausal transition are compelling (5–7, 10, 11). This may, at least in principle, warrant an FSH-blocking drug to prevent and/or treat both disorders. There is also growing evidence that reducing serum FSH using a blocking antibody in mice can lower serum cholesterol (35, 36). Furthermore, several recent observations reaffirm the rationale for the use of a FSH blocking agent not only in menopausal women, but also in men. As with male mice (19, 28, 29, 31–33),

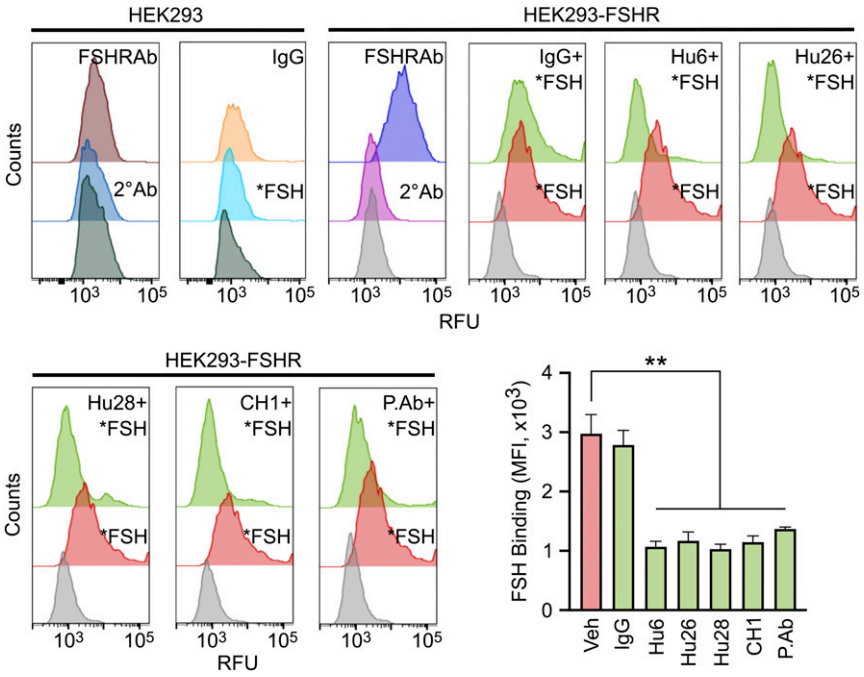

Fig. 3. Humanized antibodies block FSH binding to the FSH receptor. Representative flow cytometry histograms showing binding of Alexa647-FSH (*FSH; red) to HEK293 cells that were stably transfected to express human FSHR [confirmed by FSHR antibody (Ab; Invitrogen, PA-50963), shown in purple]. Of note is that the FSH blocking antibodies Hu6, Hu26, and H28; the mouse–human chimera CH1; and the epitope-targeted polyclonal antibody inhibited *FSH binding (light green). Gray histograms indicate no added *FSH. Expectedly, there are no shifts with FSHR Ab, secondary (2°) Ab, or *FSH in untransfected HEK293 cells. Inhibition of *FSH binding shown as median fluorescence intensity (MFI); mean ± SEM from three experiments; unpaired *t* test, $^{**}P < 0.01$. RFU, relative fluorescence unit.

suppressing serum FSH results in weight loss in men. A randomized interventional trial showed that prostate cancer patients receiving a GnRH agonist, triptorelin, which drops FSH levels, displayed lower body weight and body fat compared with those who underwent orchiectomy, where serum FSH levels are elevated (34). With that said, GnRH agonists alter other hormones, including GnRH itself, LH, activin, and inhibin, some or all of which may be important confounders depending on the target site. These inherent confounders in GnRH-based clinical trials make any negative data regarding FSH actions uninterpretable (13, 42, 43). The selective inhibition of FSH action therefore becomes a worthy imperative.

Methods

Generation of Humanized FSH Blocking Antibodies. We utilized our murine monoclonal anti-FSHβ antibody, Hf2, which was previously generated against the receptor-binding epitope of human FSHβ, namely LVYKDPARPKIQK, and validated functionally for its ability to inhibit osteoclasts, enhance bone mass, and reduce body fat (28, 29). Rapid amplification of cDNA ends (RACE) was first used to amplify the variable domains of the heavy and light IgG chains, V_H and V_L, of the Hf2 hybridoma. We then constructed a mouse–human chimeric antibody (CH1) by cloning the V_H and V_L together with human IgG_1-C_H and IgK-C_L fragments into pTT5 vector. CH1 was expressed in HEK293 cells, the supernatants purified with a protein A affinity column, and the purified antibody buffer-exchanged into PBS using a PD-10 desalting column. We then performed homology modeling on the variable domain sequences of CH1 to determine framework residues in the inner core, following which one human acceptor for V_H and V_L that shared the highest sequence homology to the mouse counterparts was selected. CDRs of CH1 were then grafted into the human acceptor framework. Single site saturation mutagenesis using NNK degenerate codons was utilized to generate a library of the antigen-binding fragments (Fabs) with mutations flanking the CDR, which were subcloned into the pFASEBA vector. The resulting 30 humanized Fab clones (1–30) were expressed in *E. coli*, and crude supernatant extracts were tested for binding to both mouse and human FSHβ in an ELISA (*SI Appendix*, Fig. 1). This was followed by further confirmation of FSH binding by SPR (Biacore 8K/T200) and rank-ordering by dissociation constants (K_ds; *SI Appendix*, Table S1). Following sequencing, cDNAs encoding three high-affinity humanized IgGs with the lowest K_ds, namely clones 6, 26, and 28, were subcloned into pTT5 vector for expression in HEK293 cells, and the resulting IgGs were purified by protein A affinity chromatography. Biacore was used to measure kinetics and binding affinity of the three purified candidates, namely Hu6, Hu26, and Hu28, and CH1 with human and mouse FSH (*SI Appendix*, Fig. S2). We also produced Fab and Fc fragments of Hu6 by papain digestion using the Pierce Fab Preparation Kit (ThermoFisher, no. 44985). The Fab fragment was separated from Fc and undigested Hu6 using Protein A agarose.

Protein Thermal Shift Assay. The thermal shift assay used a fluorescent reporter, Sypro-Orange (Applied Biosystems), to detect hydrophobic domains that are exposed following the heat-induced unfolding of globular proteins. Hu6, Hu6-Fab, or Hu6-Fc (1.5 μg/μL) was incubated with or without human FSH or human LH (both at 0.5 μg/μL) at room temperature for 30 min, with fluorescence captured sequentially at 0.3 °C increments using a StepOne Plus Thermocycler (Applied Biosystems). Tm was calculated based on the inflection point of the melt curve, and the thermal shift was derived from $\Delta Tm = Tm_{Ab+FSH(or\ LH)} - Tm_{Ab}$.

Molecular Dynamics Simulations and Fine Mapping of Antibody–FSH Interface. The crystal structure of human FSH in complex with the entire ectodomain of human FSHR (PDB ID code 4AY9) was used as a template to model mouse FSH as described before (28, 29). The sequence of mouse FSH was obtained from UniProt (α chain, ID code P01215; β chain, ID code Q60687). Using a human IgG template (PDB ID codes 1FGV and 3AUV), we constructed homology models of the variable regions of the humanized antibodies Hu6, Hu26, Hu28, and Hu23 and the chimera CH1 using Modeler (48). We confirmed stereochemical parameters using PROCHECK and PROSA (49). The interacting interface between FSHβ and each modeled structure was examined by HADDOCK (39, 40), and clusters with the lowest rmsd were selected for fine mapping. For molecular-dynamics simulations, models of the docked complexes were prepared using Protein-Prepare implemented in the HTMD suite (50). Thirteen disulphide bonds were introduced into the FSHα and FSHβ chains, and the complex was parameterized using Amberff14SB force field and solvated in a TIP3P Water Box, with edges extending ≥10 Å from the

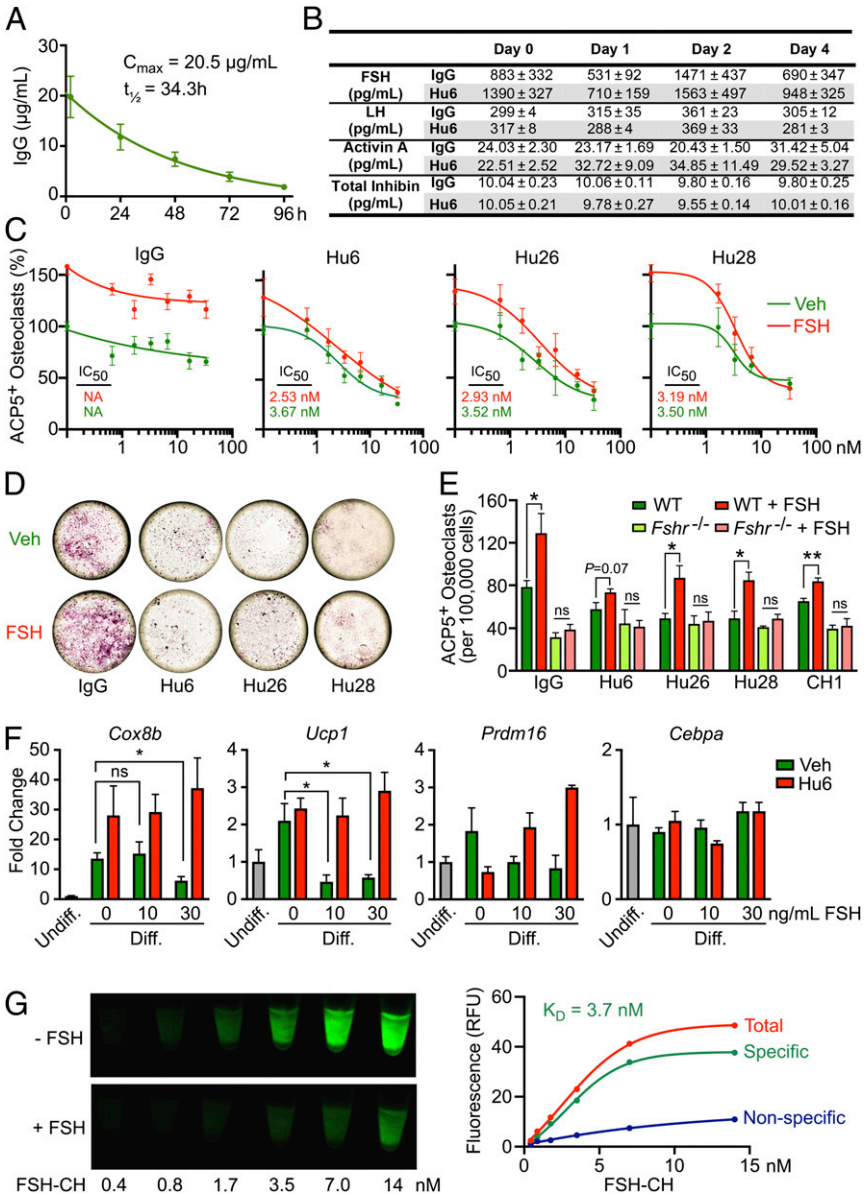

		Day 0	Day 1	Day 2	Day 4
FSH (pg/mL)	IgG	883 ± 332	531 ± 92	1471 ± 437	690 ± 347
	Hu6	1390 ± 327	710 ± 159	1563 ± 497	948 ± 325
LH (pg/mL)	IgG	299 ± 4	315 ± 35	361 ± 23	305 ± 12
	Hu6	317 ± 8	288 ± 4	369 ± 33	281 ± 3
Activin A (pg/mL)	IgG	24.03 ± 2.30	23.17 ± 1.69	20.43 ± 1.50	31.42 ± 5.04
	Hu6	22.51 ± 2.52	32.72 ± 9.09	34.85 ± 11.49	29.52 ± 3.27
Total Inhibin (pg/mL)	IgG	10.04 ± 0.23	10.06 ± 0.11	9.80 ± 0.16	9.80 ± 0.25
	Hu6	10.05 ± 0.21	9.78 ± 0.27	9.55 ± 0.14	10.01 ± 0.16

Fig. 4. Pharmacokinetic and functional studies on humanized antibodies. (*A*) Plasma C_{max} (20.5 μg/mL) and half-life ($t_{1/2}$ = 34.3 h) of Hu6 (100 μg per mouse) injected intraperitoneally into female C57BL/6 mice (n = 6). (*B*) There was no difference in serum FSH, LH, activin A, or total inhibin levels in female C57BL/6 mice following one or two injections of Hu6 (100 μg per mouse; n = 5 mice). Full concentration–response curves (*C*) and representative light micrographs for the highest antibody concentration (66 nM; *D*) displaying the inhibition of ACP5-positive osteoclast formation in bone marrow cell cultures (50 ng/mL RANKL and 20 ng/mL MCSF) in response to Hu6, Hu26, or Hu28 with or without human FSH (50 ng/mL). Calculated IC_{50}s are shown. (*E*) Inhibition by Hu6, Hu26, and Hu28 (6.6 nM) of FSH-induced osteoclastogenesis in wild type mice (with intact FSHRs) was not seen in cultures from *Fshr*$^{-/-}$ mice, proving that the antibodies act via the FSH axis. (*F*) Expression of beiging genes, namely *Cox8b*, *Ucp1*, *Prdm16*, and *Cebpa*, in response to Hu6 (6.6 nM) and/or FSH (10 or 30 ng/mL) in 3T3.L1 cell cultures under differentiating conditions (*Methods*). (*G*) 3T3-L1 cells grown in differentiation medium with 10 μM troglitazone for 8 d were incubated with FSH-CH for 2 h (37 °C) with or without a 100-fold molar excess (1.4 μM) of nonconjugated FSH. Cells were scanned using Li-Cor Scanner (800-nm channel). Scanned images (*Left*) and saturation curves based on quantitation of scanned images (*Right*) are shown (K_D = 3.7 nM).

solute. For each model, 5 ns of NPT ensemble was run to equilibrate the system, followed by a production run of 250 ns in NVE ensemble using Acemd MD engine (https://www.acellera.com/). The time step was kept at 4 fs, periodic boundary conditions were utilized, and the accuracy of the particle mesh Ewald was increased, while direct sum tolerance was reduced by an order of magnitude (0.000001). rmsd-based clustering was carried out using Biki Life Sciences Suite (51). For calculating electrostatic binding energy (ΔΔG), the medoid from the largest of the three clusters was used. Ionization states (pK_a) of the side chains were identified using PROPKA (52) as implemented on the PDB2PQR server (53). Adaptive Poisson Boltzmann equation was solved to calculate the electrostatic interactions between FSH and antibodies using APBS (54). Figures were generated using MolSoft ICM-Pro Suite (www.molsoft.com) and ezCADD (55). We first determined the CDR regions of Hu6, Hu23, Hu26, Hu28, and CH1 in silico using Kabat numbering scheme (56) and thereafter utilized GETAREA to analyze solvent accessibility of each amino acid residue of V_H and V_L (57, 58).

Flow Cytometry. We created a stable FSHR-overexpressing HEK293 cell line. FSHR protein expression was detected with Alexa 647-labeled human FSH (*FSH; 100 nM) or an anti-FSHR antibody (1 in 1,000; Invitrogen, PA-50963) by flow cytometry (CytoFLEX; Beckman Coulter). *FSH was added with or without Hu6, Hu26, Hu28, or CH1 (all at 10 μM). Untransfected cells were used as specificity controls. There were no shifts with FSHR Ab, secondary antibody, or *FSH. Median fluorescence intensity (MFI) was determined from three separate experiments.

Cell-Based Assays. To study osteoclast formation, bone marrow hematopoietic cells from wild type mice, or, to establish FSH-specificity, from *Fshr*$^{-/-}$ mice, were incubated with RANKL (100 ng/mL) and MCSF (20 ng/mL) for 5 d with or without FSH (50 ng/mL) and antibodies Hu6, Hu26, or Hu28 or human IgG (negative control). Osteoclast numbers were quantitated blindly as cells positive for tartrate-resistant acid phosphatase type 5 (ACP5) using a kit (Sigma, 386A-1KT). IC_{50}s of the three antibodies were calculated using GraphPad Prism. To study the effects of Hu6 on the expression of adipocyte beiging genes, we cultured 3T3-L1 cells in medium containing FBS (10%, vol/vol) for 3 d in submaximal (0.25×) differentiation conditions [rosiglitazone (0.5 μM), dexamethasone (0.25 μM), IBMX (0.125 mM), and insulin (2.5 μg/mL)] and for a further 9 d in insulin (2.5 μg/mL) in the presence of Hu6 with or without FSH (10 or 30 ng/mL). *Cox8b*, *Ucp1*, *Prdm16*, and *Cebpa* gene expression was studied using quantitative PCR with SYBR Green and validated primer sets as in Liu et al. (29). For cAMP measurements, differentiating 3T3.L1 cells were treated for 20 min with $FSH^{21/18}$ or FSH^{24} (30 ng/mL) in the presence of the β_3 adrenergic agonist CL316,243 (in the presence of 0.1 mM IBMX). cAMP was measured in cell extracts using an ELISA kit (Cayman, no. 581001).

Mouse Studies. For plasma half-life ($t_{1/2}$) studies, C57BL/6J mice were injected intraperitoneally with a single dose of Hu6 (100 μg), which was followed by blood draws at 2 h and thereafter at 24-h intervals. Serum Hu6 levels were measured by an in-house ELISA, in which plates were coated with goat anti-human IgG Fab antibody (200 μg per well; Invitrogen, no. 31122) and incubated with mouse serum (1:1,000) followed by capture with goat anti-human HRP-conjugated IgG (H + L) antibody (Invitrogen, A18805). C_{max} and $t_{1/2}$ were determined by fitting the time-course data to the exponential decay function. In a separate experiment, blood was drawn at day 0, following which groups of mice received either one injection or two injections 48 h apart of Hu6 or human IgG (100 μg per mouse). Serum LH, FSH, activin A, and total inhibin levels were measured using the Milliplex Map Mouse Pituitary Magnetic Bead Panel (Millipore, MPTMAG49K; Thermo Scientific, EM3RB; and R&D, LXSAHM-01, respectively). To image FSHRs in vivo, anesthetized adult female BALB/c mice (Charles River Laboratories) were placed on a stage with a venous catheter for tail vein injection of recombinant human FSH (Sigma) that was conjugated to the near-infrared II (NIR-II) fluorophore CH1055 (59). NIR-II images were acquired using a 320- × 256-pixel 2-dimensional indium gallium arsenide (InGaAs) photodiode array (Princeton Instruments). The Mount Sinai Institutional Animal Care and Use Committee and Stanford University Animal Ethics Committee approved the relevant experimental protocols.

Statistical Methods. Statistically significant differences between any two groups were examined using a two-tailed Student's *t* test, given equal variance. One-way ANOVA was used to examine statistical significance between more than two groups, followed by post hoc Bonferroni correction. *P* values were considered significant at or below 0.05.

Data Availability. All study data are included in the article and supporting information.

ACKNOWLEDGMENTS. M.Z. is grateful to the National Institutes of Health for grant support, namely U19 AG60917 (to M.Z. and C.J.R.) and R01 DK113627 (to M.Z.). M.I.N. is supported by the Maria I. New Children's Hormone Research Foundation. M.Z. is an inventor on patents on FSH, bone, and body fat regulation. These patents are owned by Icahn School of Medicine at Mount Sinai, with M.Z. being a recipient of royalties should they arise per institutional policies. M.Z. also consults for several financial platforms, including Gerson Lehrman Group and Guidepoint, on drugs for osteoporosis and genetic bone diseases.

1. International Osteoporosis Foundation, Osteoporosis–Incidence and burden. (2016). https://www.iofbonehealth.org/osteoporosis. Accessed 12 October 2020.
2. World Health Organization, Obesity and overweight. (2018). https://www.who.int/news-room/fact-sheets/detail/obesity-and-overweight. Accessed 12 October 2020.
3. M. Zaidi, C. Buettner, L. Sun, J. Iqbal, Minireview: The link between fat and bone: Does mass beget mass? *Endocrinology* **153**, 2070–2075 (2012).
4. E. A. Greco *et al*., Is obesity protective for osteoporosis? Evaluation of bone mineral density in individuals with high body mass index. *Int. J. Clin. Pract.* **64**, 817–820 (2010).
5. M. Sowers, S. Pope, G. Welch, B. Sternfeld, G. Albrecht, The association of menopause and physical functioning in women at midlife. *J. Am. Geriatr. Soc.* **49**, 1485–1492 (2001).
6. M. Sowers *et al*., Changes in body composition in women over six years at midlife: Ovarian and chronological aging. *J. Clin. Endocrinol. Metab.* **92**, 895–901 (2007).
7. M. R. Sowers *et al*., Hormone predictors of bone mineral density changes during the menopausal transition. *J. Clin. Endocrinol. Metab.* **91**, 1261–1267 (2006).
8. M. R. Sowers *et al*.; Study of Women's Health Across the Nation, The association of endogenous hormone concentrations and bone mineral density measures in pre- and perimenopausal women of four ethnic groups: SWAN. *Osteoporos. Int.* **14**, 44–52 (2003).
9. M. R. Sowers *et al*., Endogenous hormones and bone turnover markers in pre- and perimenopausal women: SWAN. *Osteoporos. Int.* **14**, 191–197 (2003).
10. J. F. Randolph Jr *et al*., Change in estradiol and follicle-stimulating hormone across the early menopausal transition: Effects of ethnicity and age. *J. Clin. Endocrinol. Metab.* **89**, 1555–1561 (2004).
11. J. F. Randolph Jr *et al*., Change in follicle-stimulating hormone and estradiol across the menopausal transition: Effect of age at the final menstrual period. *J. Clin. Endocrinol. Metab.* **96**, 746–754 (2011).
12. J. F. Randolph Jr *et al*., Reproductive hormones in the early menopausal transition: Relationship to ethnicity, body size, and menopausal status. *J. Clin. Endocrinol. Metab.* **88**, 1516–1522 (2003).
13. S. Khosla, Estrogen versus FSH effects on bone metabolism: Evidence from interventional human studies. *Endocrinology* **161**, bqaa111 (2020).
14. M. Zaidi *et al*., FSH, bone mass, body fat, and biological aging. *Endocrinology* **159**, 3503–3514 (2018).
15. E. Abe *et al*., TSH is a negative regulator of skeletal remodeling. *Cell* **115**, 151–162 (2003).
16. J. G. Cannon *et al*., Follicle-stimulating hormone, interleukin-1, and bone density in adult women. *Am. J. Physiol. Regul. Integr. Comp. Physiol.* **298**, R790–R798 (2010).
17. J. A. Stilley *et al*., FSH receptor (FSHR) expression in human extragonadal reproductive tissues and the developing placenta, and the impact of its deletion on pregnancy in mice. *Biol. Reprod.* **91**, 74 (2014).
18. L. Sun *et al*., Oxytocin regulates body composition. *Proc. Natl. Acad. Sci. U.S.A.* **116**, 26808–26815 (2019).
19. L. Sun *et al*., FSH directly regulates bone mass. *Cell* **125**, 247–260 (2006).
20. L. Sun *et al*., Functions of vasopressin and oxytocin in bone mass regulation. *Proc. Natl. Acad. Sci. U.S.A.* **113**, 164–169 (2016).
21. R. Tamma *et al*., Oxytocin is an anabolic bone hormone. *Proc. Natl. Acad. Sci. U.S.A.* **106**, 7149–7154 (2009).
22. J. Wang *et al*., Follicle-stimulating hormone increases the risk of postmenopausal osteoporosis by stimulating osteoclast differentiation. *PLoS One* **10**, e0134986 (2015).
23. M. Zaidi, Skeletal remodeling in health and disease. *Nat. Med.* **13**, 791–801 (2007).
24. M. Zaidi *et al*., Actions of pituitary hormones beyond traditional targets. *J. Endocrinol.* **237**, R83–R98 (2018).
25. L. J. Robinson *et al*., FSH-receptor isoforms and FSH-dependent gene transcription in human monocytes and osteoclasts. *Biochem. Biophys. Res. Commun.* **394**, 12–17 (2010).
26. E. Cheung *et al*., Bone loss during menopausal transition among southern Chinese women. *Maturitas* **69**, 50–56 (2011).
27. D. Rendina *et al*., FSHR gene polymorphisms influence bone mineral density and bone turnover in postmenopausal women. *Eur. J. Endocrinol.* **163**, 165–172 (2010).
28. Y. Ji *et al*., Epitope-specific monoclonal antibodies to FSHβ increase bone mass. *Proc. Natl. Acad. Sci. U.S.A.* **115**, 2192–2197 (2018).
29. P. Liu *et al*., Blocking FSH induces thermogenic adipose tissue and reduces body fat. *Nature* **546**, 107–112 (2017).
30. L. L. Zhu *et al*., Blocking FSH action attenuates osteoclastogenesis. *Biochem. Biophys. Res. Commun.* **422**, 54–58 (2012).
31. L. L. Zhu *et al*., Blocking antibody to the β-subunit of FSH prevents bone loss by inhibiting bone resorption and stimulating bone synthesis. *Proc. Natl. Acad. Sci. U.S.A.* **109**, 14574–14579 (2012).
32. X. Han *et al*., A novel follicle-stimulating hormone vaccine for controlling fat accumulation. *Theriogenology* **148**, 103–111 (2020).
33. W. Geng *et al*., Immunization with FSHβ fusion protein antigen prevents bone loss in a rat ovariectomy-induced osteoporosis model. *Biochem. Biophys. Res. Commun.* **434**, 280–286 (2013).
34. P. B. Østergren *et al*., Luteinizing hormone-releasing hormone agonists are superior to subcapsular orchiectomy in lowering testosterone levels of men with prostate cancer: Results from a randomized clinical trial. *J. Urol.* **197**, 1441–1447 (2017).
35. Y. Guo *et al*., Blocking FSH inhibits hepatic cholesterol biosynthesis and reduces serum cholesterol. *Cell Res.* **29**, 151–166 (2019).
36. Y. Song *et al*., Follicle-stimulating hormone induces postmenopausal dyslipidemia through inhibiting hepatic cholesterol metabolism. *J. Clin. Endocrinol. Metab.* **101**, 254–263 (2016).
37. G. R. Bousfield *et al*., Macro- and micro-heterogeneity in pituitary and urinary follicle-stimulating hormone glycosylation. *J. Glycomics Lipidomics* **4**, 1000125 (2014).
38. B. Webb, A. Sali, Comparative protein structure modeling using MODELLER. *Curr Protoc Bioinformatics* **54**, 5.6.1–5.6.37 (2016).
39. G. C. P. van Zundert *et al*., The HADDOCK2.2 web server: User-friendly integrative modeling of biomolecular complexes. *J. Mol. Biol.* **428**, 720–725 (2016).
40. T. A. Wassenaar *et al*., WeNMR: Structural biology on the grid. *J. Grid Comput.* **10**, 743–767 (2012).
41. T. R. Kumar, Y. Wang, N. Lu, M. M. Matzuk, Follicle stimulating hormone is required for ovarian follicle maturation but not male fertility. *Nat. Genet.* **15**, 201–204 (1997).
42. M. T. Drake, L. K. McCready, K. A. Hoey, E. J. Atkinson, S. Khosla, Effects of suppression of follicle-stimulating hormone secretion on bone resorption markers in postmenopausal women. *J. Clin. Endocrinol. Metab.* **95**, 5063–5068 (2010).
43. A. V. Uihlein, J. S. Finkelstein, H. Lee, B. Z. Leder, FSH suppression does not affect bone turnover in eugonadal men. *J. Clin. Endocrinol. Metab.* **99**, 2510–2515 (2014).

44. A. M. Akbar, L. E. Reichert Jr, T. G. Dunn, C. C. Kaltenbach, G. D. Niswender, Serum levels of follicle-stimulating hormone during the bovine estrous cycle. *J. Anim. Sci.* **39**, 360–365 (1974).
45. H. Cui *et al*., FSH stimulates lipid biosynthesis in chicken adipose tissue by upregulating the expression of its receptor FSHR. *J. Lipid Res.* **53**, 909–917 (2012).
46. X. M. Liu *et al*., FSH regulates fat accumulation and redistribution in aging through the Gαi/Ca(2+)/CREB pathway. *Aging Cell* **14**, 409–420 (2015).
47. Genentech. Herceptin. Herceptin (Package Insert). (1998). https://www.accessdata.fda.gov/drugsatfda_docs/label/1998/trasgen092598lb.pdf. Accessed 12 October 2020.
48. A. Fiser, A. Sali, Modeller: Generation and refinement of homology-based protein structure models. *Methods Enzymol.* **374**, 461–491 (2003).
49. M. Wiederstein, M. J. Sippl, ProSA-web: Interactive web service for the recognition of errors in three-dimensional structures of proteins. *Nucleic Acids Res.* **35**, W407–W410 (2007).
50. S. Doerr, M. J. Harvey, F. Noé, G. De Fabritiis, HTMD: High-throughput molecular dynamics for molecular discovery. *J. Chem. Theory Comput.* **12**, 1845–1852 (2016).
51. S. Decherchi, G. Bottegoni, A. Spitaleri, W. Rocchia, A. Cavalli, BiKi life Sciences: A new suite for molecular dynamics and related methods in drug discovery. *J. Chem. Inf. Model.* **58**, 219–224 (2018).
52. M. H. Olsson, C. R. Søndergaard, M. Rostkowski, J. H. Jensen, PROPKA3: Consistent treatment of internal and surface residues in empirical pKa predictions. *J. Chem. Theory Comput.* **7**, 525–537 (2011).
53. T. J. Dolinsky, J. E. Nielsen, J. A. McCammon, N. A. Baker, PDB2PQR: An automated pipeline for the setup of Poisson-Boltzmann electrostatics calculations. *Nucleic Acids Res.* **32**, W665–W667 (2004).
54. E. Jurrus *et al*., Improvements to the APBS biomolecular solvation software suite. *Protein Sci.* **27**, 112–128 (2018).
55. A. Tao *et al*., ezCADD: A rapid 2D/3D visualization-enabled web modeling environment for democratizing computer-aided drug design. *J. Chem. Inf. Model.* **59**, 18–24 (2019).
56. Andrew Martin's Group, Kabat numbering scheme. Kabatnum. http://www.bioinf.org.uk/abs/info.html. Accessed 12 October 2020.
57. R. Fraczkiewicz, W. Braun, Exact and efficient analytical calculation of the accessible surface areas and their gradients for macromolecules. *J. Comput. Chem.* **19**, 319–333 (1998).
58. S. Negi, H. Zhu, R. Fraczkiewicz, W. Braun, Calculation of solvent accessible surface areas, atomic solvation energies and their gradients for macromolecules. http://curie.utmb.edu/getarea.html. Accessed 12 October 2020.
59. Y. Feng *et al*., Live imaging of follicle stimulating hormone receptors in gonads and bones using near infrared II fluorophore. *Chem. Sci.* **8**, 3703–3711 (2017).